

## Photoluminescence and Raman Spectroscopy Study on Color Centers of Helium Ion-Implanted 4H-SiC

Song, Y.; Xu, Z.; Li, R.; Wang, H.; Fan, Y.; Rommel, M.; Liu, J.; Astakhov, G.; Hlawacek, G.; Li, B.; Xu, J.; Fang, F.;

Originally published:

September 2020

**Nanomanufacturing and Metrology 3(2020), 205-217**

DOI: <https://doi.org/10.1007/s41871-020-00061-8>

Perma-Link to Publication Repository of HZDR:

<https://www.hzdr.de/publications/Publ-31451>

Release of the secondary publication  
on the basis of the German Copyright Law § 38 Section 4.

# Photo-luminescence and Raman spectroscopy study on color centers of helium ion implanted 4H-SiC

Ying Song<sup>1</sup>, Zongwei Xu<sup>1\*</sup>, Rongrong Li<sup>2</sup>, Hong Wang<sup>3</sup>, Yexin Fan<sup>1</sup>, Mathias Rommel<sup>4\*</sup>, Jiayu Liu<sup>1</sup>, Georgy Astakhov<sup>5</sup>, Gregor Hlawacek<sup>5</sup>, Bingsheng Li<sup>6</sup>, Jun Xu<sup>2</sup>, Fengzhou Fang<sup>1\*</sup>

(1 State Key Laboratory of Precision Measuring Technology & Instruments, Centre of MicroNano Manufacturing Technology, Tianjin University, Tianjin 300072, China

2 State Key Laboratory for Mesoscopic Physics and Electron Microscopy Laboratory, School of Physics, Peking University, Beijing 100871, China

3 State Key Laboratory of Separation Membranes and Membrane Processes, Tianjin Polytechnic University, China

4 Fraunhofer Institute for Integrated Systems and Device Technology (IISB), Schottkystrasse 10, Erlangen 91058, Germany

5 Institute of Ion Beam Physics Materials Research (HZDR), Bautzner Landstrasse 400, Dresden 01328, Germany

6 Institute of Modern Physics, Chinese Academy of Sciences, Lanzhou, Gansu 730000, China

\* Corresponding e-mail: [zongweixu@tju.edu.cn](mailto:zongweixu@tju.edu.cn), [mathias.rommel@iisb.fraunhofer.de](mailto:mathias.rommel@iisb.fraunhofer.de), [fzfang@tju.edu.cn](mailto:fzfang@tju.edu.cn)

---

Received: August XX, 201X / Accepted: August XX, 201X/Accepted: August XX, 201X/Published online: August XX, 201X

---

## Abstract:

*Color centers in silicon carbide (SiC) are promising candidates for quantum technologies. However, the richness of the polytype and defect configuration of SiC makes the accurate control of the types and position of defects in SiC still be challenging. In this study, helium ion implanted 4H-SiC was characterized by atomic force microscopy (AFM), confocal photo-luminescence (PL) and Raman spectroscopy at room temperature. PL signals of silicon vacancy were found using 638 nm and 785 nm laser excitation by means of depth profiling and SWIFT mapping. Lattice defect (C-C bond) were detected by continuous laser excitation at 532 nm and 638 nm, respectively. The PL / Raman depth profiling is helpful to reveal the three-dimensional distribution of produced defects. Differences between the depth profiling results and SRIM simulation results were explained by considering the depth resolution of the confocal measurement setup, helium bubbles and swelling.*

**Keywords :** Helium ion implantation; Silicon carbide (SiC); Color center; Point defect; Silicon vacancy; Confocal photo-luminescence spectroscopy; Raman spectroscopy; Atomic force microscopy (AFM)

---

## 1. Introduction

Increasing demands in data storage, processing efficiency and transmission security promote the development of quantum technologies. Solid state spin is one promising candidate for quantum technologies thanks to its robustness and compatibility with the preparation process of semiconductor devices. Color centers in diamond, especially the negatively charged nitrogen vacancy center (NV<sup>-</sup>) in diamond have initiated abundant fundamental research and quantum applications in the last years [1-3]. Silicon carbide (SiC) is an important wide-bandgap semiconductor material for high-power electronics and high-temperature applications [4,5]. Recently, similar to the properties of NV<sup>-</sup> in diamond, point defects with spin characteristic in SiC such as silicon vacancy (V<sub>Si</sub>) also received extensive attentions for their superior characteristics, and can be widely used in ultra-sensitive quantum sensing such as temperature [6], magnetic field [7] sensing and etc. Compared with color centers in diamond, spin defects in SiC have many outstanding properties. For instance, the microfabrication technique of SiC is much more mature than that of diamond because of its use for commercially available electron devices. Defects in silicon carbide have been explored as promising spin systems in quantum technologies. SiC can host single-point defects with long spin coherence times, making it promising for long-lived qubits [8]. The emission of the point defects due to the formation of deep levels in the bandgap make them candidates of single photon source which can be used in quantum communication [9] and in vivo bio-imaging [10].

The generation and detection of color centers is very important in quantum key distribution and photonic quantum information processing [1]. Point defect structures in SiC have been fabricated by energetic particles beam methods, including electron irradiation [8], proton beam writing [11,12], direct femtosecond laser writing [13], and ion beam implantation [14]. The characterization of the emission properties is also important for both, understanding the electrical structures of the energy band and the application. Castelletto reported a silicon carbide room-temperature single-photon source which is composed of an intrinsic defect,  $C_{Si}V_C$ , known as the carbon anti-site vacancy pair, and which has an emission at around 700 nm at room temperature [15]. Koehl showed that several neutrally charged carbon–silicon divacancies in 4H-SiC can be optically addressed at temperatures ranging from 20 to 300 K, which are optically active near telecommunication wavelengths [16]. Zargaleh demonstrated that the negatively charged NV center can be fabricated in  $2 \times 10^{16} \text{ cm}^{-3}$  nitrogen doped n-type 3C-SiC by using high energy proton (6 MeV) irradiation, where the zero-phonon lines (ZPL) of  $NV^-$  center in 3C-SiC are shifted from the visible to the near infrared at around 1400 nm [12]. And single silicon vacancies  $V_{Si}$  were proved to have emission in the range of 850-950 nm at room temperature [17,18]. Due to the small diffusion coefficient of impurities in silicon carbide, ion implantation has become the main method of deliberate doping for silicon carbide and has developed into a popular color center preparation method in recent years. Al Atem et al. produced color centers in 3C-SiC using ion implantation with annealing of Ar ions, He ions and H ions, respectively. It was found that H ions are more likely to produce double vacancy defects [19]. Cottom et al. prepared the  $N_C V_{Si}$  color center by N ion and Al ion implantation into 4H-SiC [20]. Recently, the group of Xu presented a method to precisely control the depths of the ion implantation induced shallow silicon vacancy defects in silicon carbide by using reactive ion etching with little surface damage [21].

Improving the yield and position accuracy of the color center is an attractive topic. Wang et al. show that the helium ion implantation has a higher production efficiency of silicon vacancies than carbon or hydrogen implantation [22]. However, for He ion implantation using helium ion microscope (HIM), ion beam channeling effects should be carefully considered when the HIM beam energy is larger than around 15 keV [23]. While improving the color center yield, it is also necessary to control the purity of surrounding lattice to ensure the quality of the color center (such as coherence time). Thus, high-quality homo-epitaxial SiC wafers are usually used as the host material for color centers [19] and post-annealing processes are considered to reduce the lattice damage and improve the lifetime of the color centers [24]. Raman spectroscopy is a fast and non-destructive method to characterize lattice defects. Ali et al. found  $sp^2/sp^3$  C-C vibration Raman bond between 1400-1600  $\text{cm}^{-1}$  (D band range of carbon material) in 30 keV He ion implanted 4H and 6H-SiC [25]. Blue shift of D band with increasing excitation wavelength was found in graphite and other carbon materials [26].

Although many studies showed the photoluminescence of point defects in silicon carbide, little attention has been paid to the three-dimensional distribution of the defects. In this study, by means of 2D mapping and depth profiling, defects of helium ion implanted 4H-SiC were characterized by confocal photo-luminescence (PL) and Raman spectroscopy.  $V_{Si}$  defect PL peaks in the range of 850-950 nm were observed for the excitation with 638 nm laser and 785 nm laser. At high implantation doses, C-C Raman bands in the range of 1200-1600  $\text{cm}^{-1}$  were detected for the excitation of 532 nm and 638 nm continuous lasers.

## 2. Experimental setups

Nitrogen doped (0001) 4H-SiC substrate with  $4^\circ \pm 0.5^\circ$  off-axis from Xiamen Powerway Advanced Material Co., Ltd. (PAM-XIAMEN) was processed by helium ion implantation using a helium ion microscope, ORION NanoFab, with an energy of 30 keV, a current of 3.8 pA, a dwell time of 0.1  $\mu\text{s}$  and a beam overlap of 50% at around 300 K. Helium ion's implantation angle was chosen with 0 degree (along the normal direction of substrate,  $4^\circ$  with respect to (0001)). Each implanted region had an area of  $6 \mu\text{m} \times 6 \mu\text{m}$ . The distance between the implanted regions was about 100  $\mu\text{m}$ . Implanted regions with different doses were labeled R1-R9, as shown in Table 1 and Fig. 1. In order to accurately locate the positions of low ion dose of R1 and R2 during the spectra measurements, two marks were fabricated around the implanted areas in advance by FIB milling using Gallium ion beam with an energy of 30 keV and a current of 0.44 nA, as shown in Fig. 1. The distance between marks and the He implanted regions was sufficiently large to avoid any influence of Ga patterning on the characteristics of R1 and R2 [27].

Microscopic morphology of the ion-implanted areas with different doses was characterized by Dimension Icon atomic force microscopy (AFM) from Bruker. The pristine and implanted regions were scanned over an area of around  $100 \mu\text{m}^2$  using a non-contact tapping mode. Photoluminescence spectra and Raman spectra were measured using Horiba XploRA Plus confocal microscope in backscattering geometric configuration at room temperature. The PL/Raman spectra were excited by continuous laser excitation at 532 nm (6.69 mW), 638 nm (9.53 mW) and 785 nm (93.10 mW), respectively. 100 $\times$  objective lens with numerical aperture (NA) of 0.9, 100  $\mu\text{m}$  confocal pinhole diameter and 600 lines/mm grating were used. At the excitation of each wavelength, a single spectrum focusing on the sample surface, depth profiles focusing on different depths of the sample (from deep inside the sample to the air above the sample), and 2D mapping were all measured. 2D mapping in SWIFT<sup>TM</sup> working mode (ultra-fast Raman imaging) and depth profiling were achieved by automatically adjusting the sample stage with a displacement accuracy of 0.1  $\mu\text{m}$ , in which the XY plane is closely parallel to the surface of the 4H-SiC substrate. Acquisition time in standard working mode (including single spectrum and depth profiling measurement) for each spectrum was 10 s for 2 accumulations. And acquisition time in SWIFT<sup>TM</sup> working mode for spectrum of each point was 1 s for 1 accumulation. For all 2D maps of  $V_{Si}$ , the maximum value of the spectrum in the range of 875-950 nm is defined as the peak intensity of the silicon vacancy.

**Table 1.** Helium ion implanted n-type 4H-SiC regions with different doses

Label	Dose (ions/ $\text{cm}^2$ )
-------	-----------------------------

R1	$1.0 \times 10^{14}$
R2	$5.0 \times 10^{14}$
R3	$3.0 \times 10^{15}$
R4	$1.1 \times 10^{16}$
R5	$1.5 \times 10^{16}$
R6	$1.0 \times 10^{17}$
R7	$1.5 \times 10^{17}$
R8	$5.0 \times 10^{17}$
R9	$1.0 \times 10^{18}$

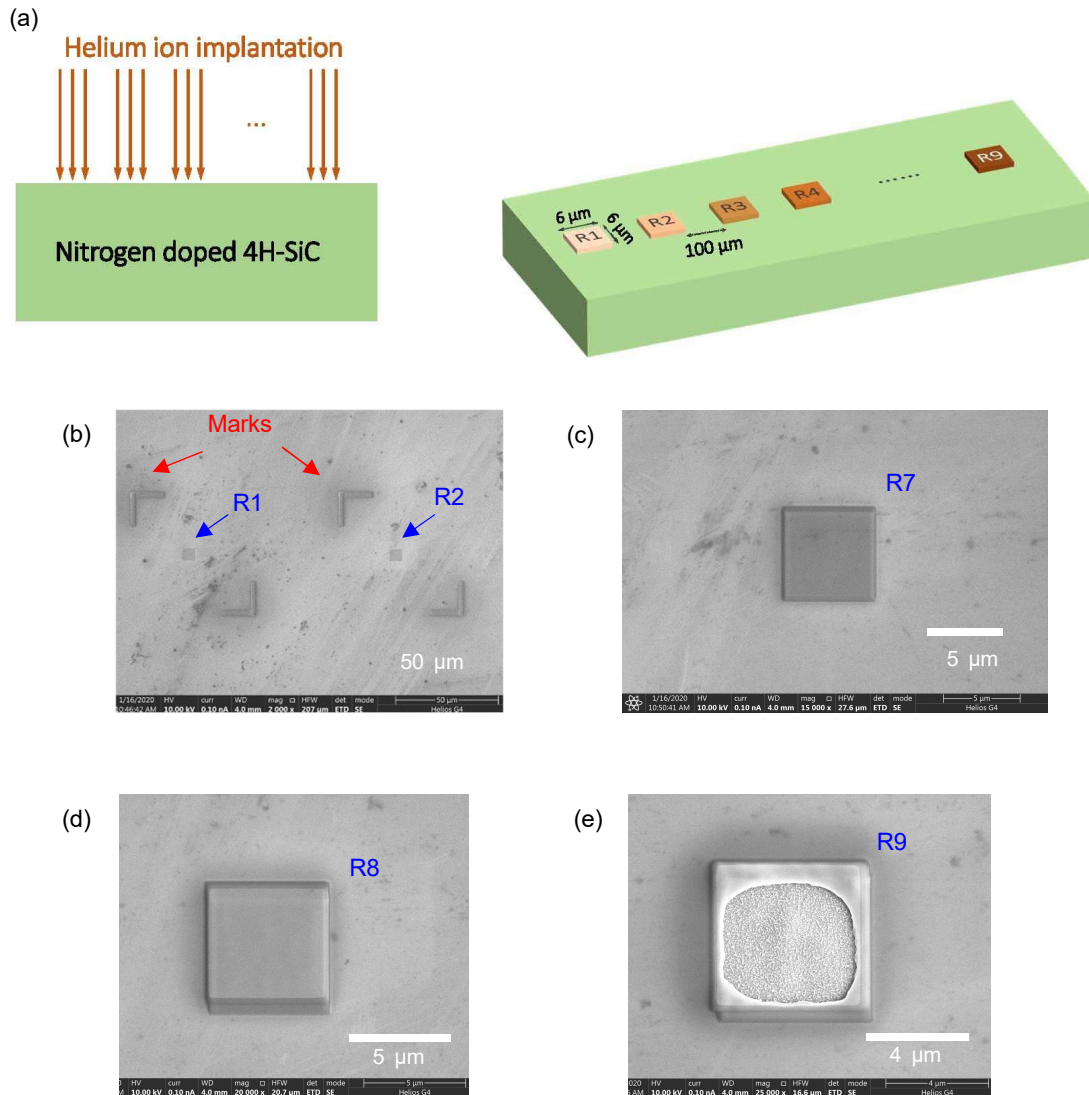


Fig. 1. Helium ion implanted regions (R1-R9) in nitrogen-doped 4H-SiC. (a) Schematic diagram of helium ion implantation positions for different ion doses of R1-R9. (b), (c), (d) and (e) show SEM images of helium ion implanted regions R1 & R2 (together with the Ga FIB-prepared marks), R7, R8, and R9, respectively.

### 3. Results and discussions

#### 3.1 Surface morphology by AFM

Surface morphology of ion-implanted areas was characterized by atomic force microscope (AFM). Fig. 2(a)-(g) shows the three-dimensional topography maps and the cross-sectional profiles for regions irradiated with doses in the range of  $3.0 \times 10^{15}$  ions/cm<sup>2</sup> –  $1.0 \times 10^{18}$  ions/cm<sup>2</sup> (R3-R9).

After ion-implantation, it can be observed from the AFM results that the topography of the irradiated regions with respect to the virgin sample surface will change. For doses lower than  $1.5 \times 10^{16}$  ions/cm<sup>2</sup>, an uplift of ~6-15 nm in the implanted region is observed compared to the virgin area. At this dose, the material has not been amorphized and point defects are the main form of damage. Implanted helium atoms, the formation of point defects (interstitials and vacancies) and clusters will induce a normal strain which is attributed to the volume change of the implanted area [28]. When the implantation dose is increased further, more damage will be introduced, and amorphous transition and helium bubbles will appear in the damaged regions. For a dose of  $1 \times 10^{17}$  ions/cm<sup>2</sup>, Leclerc has observed helium bubbles with size of 1-2 nm in the amorphous region by cross-sectional transmission electron microscopy (XTEM) [29]. Helium bubble clusters were found after room temperature He implantation (with an energy of 40 keV) and annealing at 1173 K with a dose to of  $5 \times 10^{15}$  ions/cm<sup>2</sup> [30]. Amorphous transition of SiC after helium ion implantation occurs between  $1 \times 10^{16}$  ions/cm<sup>2</sup> and  $2 \times 10^{16}$  ions/cm<sup>2</sup> at room temperature, which will lead to a swelling of around 15% because of the decrease in the density after the material becomes amorphous [29,31]. Thus, when the dose equals or exceeds  $1.5 \times 10^{16}$  ions/cm<sup>2</sup>, swelling effect is more obvious and reaches its maximum at  $5.0 \times 10^{17}$  ions/cm<sup>2</sup> (R8). Besides, significantly different from Ga ion implantation [32], for R5-R9, the edge of the ion-implanted area is higher than the center of the implanted area which may be due to the relatively large strain difference between the uplift of the helium bubble area and the virgin area. And the non-linear growth of He bubbles has been observed earlier and is a result of coalescence of nanobubbles into microbubbles, so the height of the bulge also increases with increasing implantation dose, as shown in Fig. 2(h). High concentration of helium bubbles will seriously reduce the strength of the material and promote the embrittlement of the material. As the dose further increases to  $1.0 \times 10^{18}$  ions/cm<sup>2</sup>, helium bubbles burst in the center part of the implanted area and removal of the surface material can be observed.

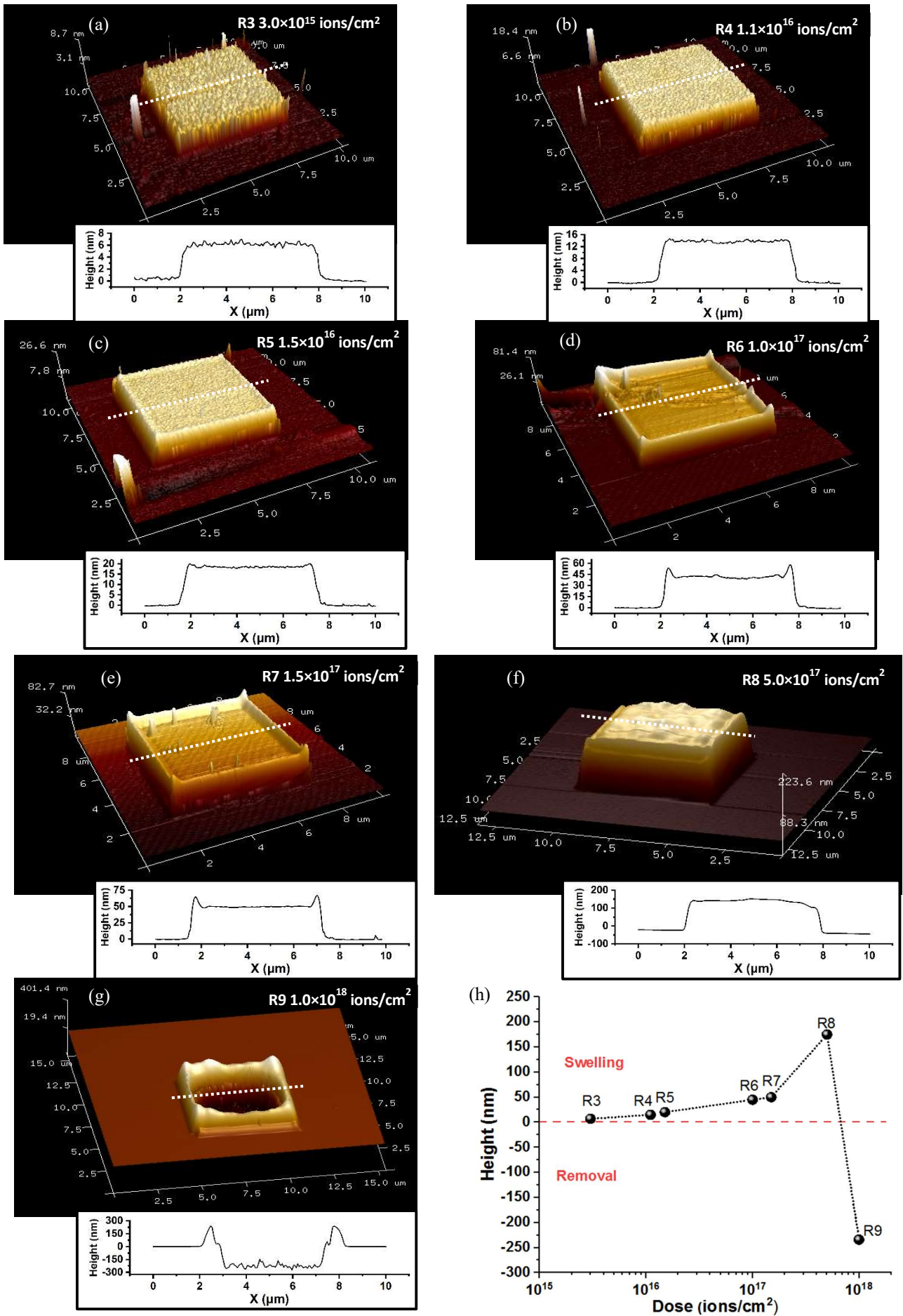


Fig. 2. Surface morphology of He ion implanted areas with different doses. Figures (a)-(g) show the surface morphology of R3-R9, and the

insert graphs are the height profiles along the dashed lines indicated in the three-dimensional morphology. (h) is the height at the center point of each area (R3-R9) in which the height of 0  $\mu\text{m}$  is the surface of the virgin area.

### 3.2 Silicon vacancy ( $V_{\text{Si}}$ )

Silicon vacancy is a kind of primary defect in SiC material. As an intrinsic defect, numerous studies have shown that silicon vacancy  $V_{\text{Si}}$  in 4H-SiC fluoresces in the range of 850-950 nm at room temperature [17,18]. In this study, only the Raman modes of 4H-SiC appeared in the spectrum of the un-irradiated region, while an emission located in the range of 850-950 nm is observed and identified as  $V_{\text{Si}}$  under the excitation for both 638 nm and 785 nm laser at room temperature, as shown in Fig. 3(c). In backscattering geometric configuration,  $E_2$  mode of the silicon carbide material is the active Raman mode [33], which has the same Raman shift at  $776\text{ cm}^{-1}$  for excitation at different wavelengths, as shown in Fig. 3(a). And for  $V_{\text{Si}}$ , the wavelength range of its emission (850-950 nm) is unchanged at different excitation wavelengths (for example, at 633 nm [34] excitation, 730 nm excitation [17] or 740 nm excitation [18]). Hain found the excitation efficiency of  $V_{\text{Si}}$  changes for different excitation wavelengths and an optimal excitation wavelength was found at around 770 nm by photoluminescence excitation measurements (PLE)[34]. The signal excited by the 785 nm laser is stronger, which may be related to the higher laser power of the 785 nm laser and the different excitation efficiency for different wavelengths[34].

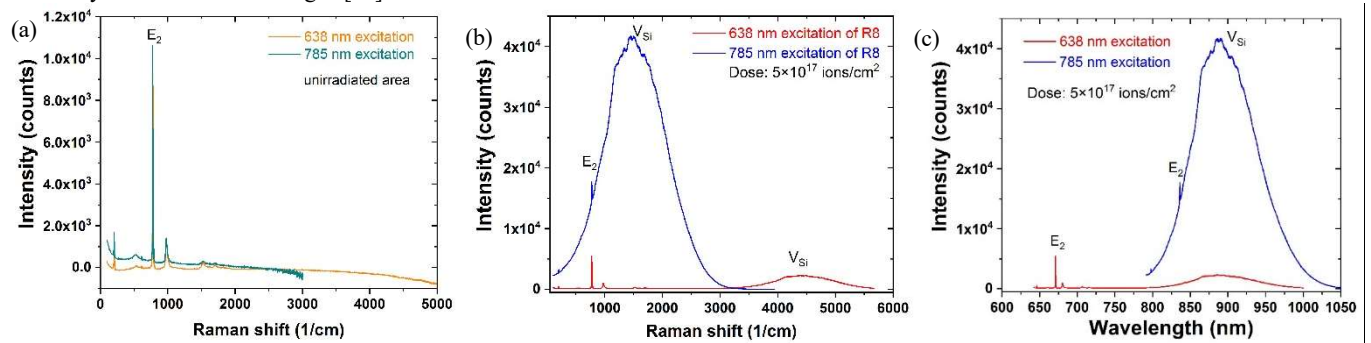


Fig. 3. PL/Raman spectra of un-irradiated area and He ion implanted area with a dose of  $5 \times 10^{17}$  ions/cm<sup>2</sup> (R8) under the excitation of 638 nm and 785 nm. (a) 638 nm and 785 nm excited spectra of un-irradiated area in Raman shift (cm<sup>-1</sup>). (b) 638 nm and 785 nm excited spectra of R8 in Raman shift (cm<sup>-1</sup>). (c) 638 nm and 785 nm excited spectra of R8 in wavelength (nm).

In order to investigate the color center distribution of the ion implanted area with different implantation doses in more detail, 2D mapping and depth profiling were measured.

#### 3.2.1 2D mapping of $V_{\text{Si}}$

Firstly, 2D SWIFT mapping in XY plane focusing on the surface of the implanted areas with different doses (R3-R8) were obtained by collecting spectra at each point of a 20 × 20 points array. Spectra were collected at each point and the  $V_{\text{Si}}$  intensity of different points was presented according to the actual spatial distribution of the points array, as shown in Fig.4. The intensity of silicon vacancies is defined as the maximum value of the spectrum in the range of 875-950 nm. Comparing the 2D mapping of  $V_{\text{Si}}$  intensity with different implantation doses of R3-R8, the distribution of the silicon vacancy changes as increasing dose when focusing on the surface of the sample. At low dose of  $3.0 \times 10^{15}$  ions/cm<sup>2</sup> (R3), point defects including silicon vacancies, carbon vacancies and other interstitial defects are produced and no obvious amorphous transition was found when performing the He<sup>+</sup> implantation at room temperature [28]. In this case, damage will be concentrated in the implanted area, thus the center of the implanted area has a stronger  $V_{\text{Si}}$  PL intensity than surrounding part, which indicates that the center part has a higher  $V_{\text{Si}}$  concentration at such a dose of  $3.0 \times 10^{15}$  ions/cm<sup>2</sup>. When the dose exceeds  $5.0 \times 10^{15}$  ions/cm<sup>2</sup>, for R4-R8, helium bubbles may have formed in the central area of the implanted region and the existence of He-vacancy complexes might have weakened the intensity of the silicon vacancy signal in the central part. At the same time, the concentration of helium bubbles in the surrounding part of the implanted area is not as high as the central area, and much more free silicon vacancy will be able to exist steadily instead of forming the He-vacancy complex. Therefore, more  $V_{\text{Si}}$  signals can be detected in the surrounding part and the 2D mapping results shows a distribution of weak signal in the middle and a strong signal around.

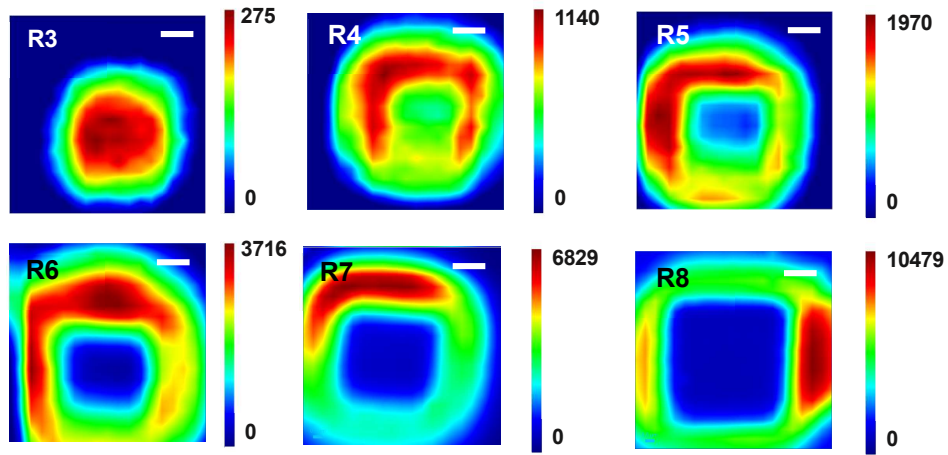


Fig. 4. 2D mapping of silicon vacancy  $V_{Si}$  PL intensity in He ion implanted 4H-SiC with different doses (R3-R8) by HIM under the excitation of 785 nm (the scale bar is 2  $\mu\text{m}$ ).

### 3.2.2 2D maps of $V_{Si}$ PL signal at different depths

Then, 2D SWIFT maps of  $V_{Si}$  intensity were measured at different depths in R3 ( $3.0 \times 10^{15}$  ions/cm<sup>2</sup>) and R8 region ( $5.0 \times 10^{17}$  ions/cm<sup>2</sup>) under the excitation of 785 nm, as shown in Fig. 5 and Fig. 6. At dose of  $3.0 \times 10^{15}$  ions/cm<sup>2</sup>, as shown in Fig. 5, the intensity of  $V_{Si}$  at different depths is always high in the center of the implanted area and weak in the surrounding area. This is because the damage at this dose is mainly point defects, and the point defects are concentrated in the center of the implanted area. As the depth of focus moves inside the sample, the intensity of the  $V_{Si}$  becomes weaker and the distribution range also decreases. This indicates that the lateral projection range of  $V_{Si}$  gradually decreases from the surface to deep inside of the sample. At the dose of  $5 \times 10^{17}$  ions/cm<sup>2</sup>, as shown in Fig. 6, amorphized material and helium bubbles already exist in the central part of the implanted region. Thus, the  $V_{Si}$  PL intensity is weak in the central implanted area at all depths. The maximum intensity of  $V_{Si}$  appears when focusing on the surface of the area around implanted zone ( $Z = 0 \mu\text{m}$ ). When focusing at 3  $\mu\text{m}$  below the surface ( $Z = -3 \mu\text{m}$ ), the PL intensity of  $V_{Si}$  decreases significantly and the weak signal area in the center indicated by the white dotted arrow also decreases compared to that on the surface. This change in distribution of  $V_{Si}$  PL signal is assumed to be related to the projected range of helium bubbles (or He-vacancy complex) in XY direction at different depths. As the focal plane moves deeper, the damage become less serious, and the form of damage changes from amorphous to point defects.

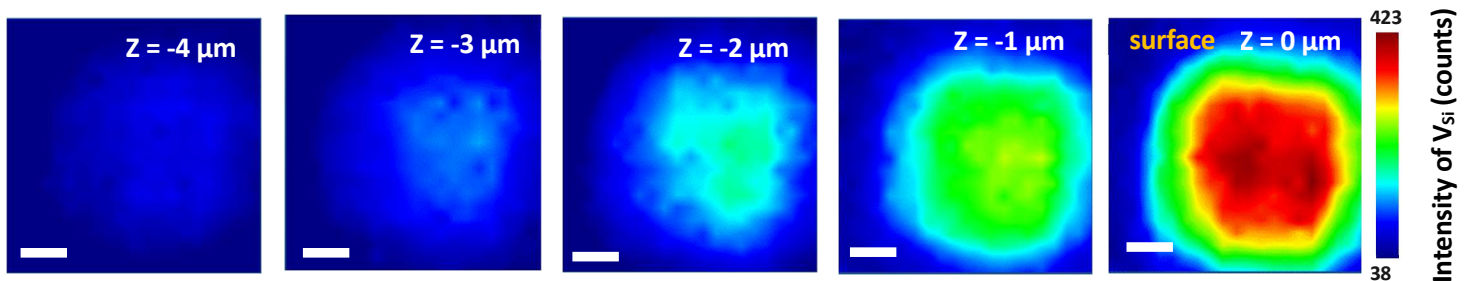


Fig. 5. 2D SWIFT mapping of  $V_{Si}$  PL intensity in R3 region at different depths. The intensity of each image is normalized with the strongest intensity at  $Z=0 \mu\text{m}$  (sample surface). (The scale bar is 2  $\mu\text{m}$ )

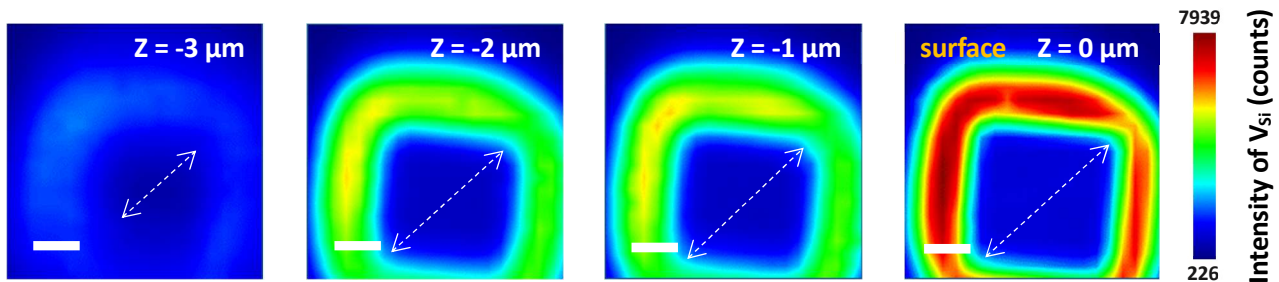


Fig. 6. 2D SWIFT mapping of  $V_{Si}$  PL intensity in R8 region at different depths. The intensity of each image is normalized with the strongest intensity at  $Z=0 \mu\text{m}$  (sample surface). (The scale bar is 2  $\mu\text{m}$  and the white dotted arrows represent the range of the central weak  $V_{Si}$  signal area).

### 3.2.3 SRIM simulation

SRIM 2013 software [35] is a Monte Carlo based simulation approach which provides the quantitative evaluation of how ions lose energy in matter and what is the distribution of ions and intrinsic point defects in the target after implantation. SRIM simulation results were performed to further explain the PL depth profiling results. The detailed parameters used in SRIM simulation are shown in Table 2 and Supplementary Material. In Fig. 7(a), the Monte Carlo simulation for 500000 helium ions with ion energy of 30 keV shows that the damage distribution in depth direction would be no deeper than 360 nm without accounting for the possible material swelling partially caused by the formation of helium bubble during high dose helium ion implantation into the semiconductor substrate [36]. And Fig. 7(b) indicates that the vacancy concentration produced by the helium ion implantation shows a peak at a depth of around 170 nm and no significant vacancy damage occurred below 300 nm from the sample surface.

**Table 2.** Parameters used in SRIM calculation

Ion type	He <sup>+</sup>	
Ion energy (keV)	30	
Ion angle (degree)	0	
Number of ions	500000	
Density of SiC target (g/cm <sup>3</sup> )	3.21	
Displacement energy (eV) [27,28]	Si	35
	C	20

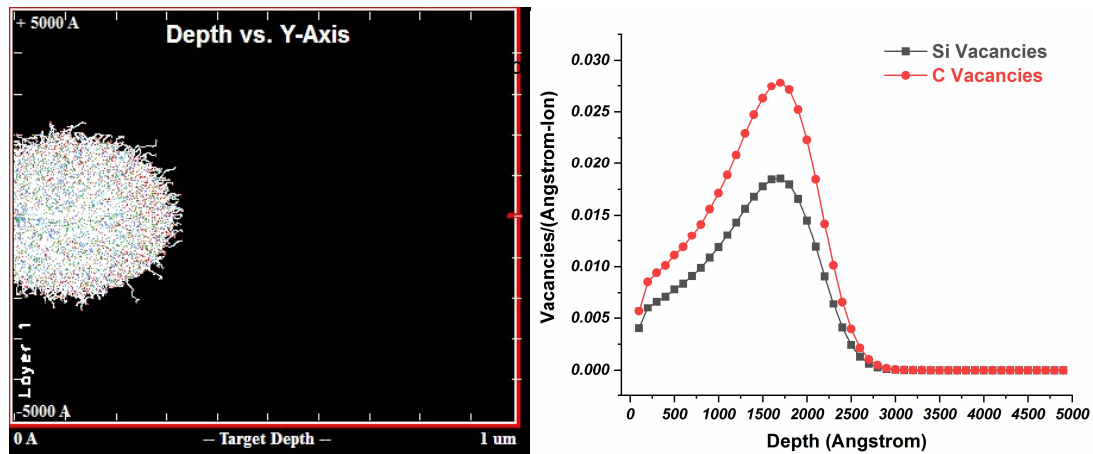


Fig. 7. The distribution of 30 keV helium ion implantation induced defects simulated by Monte Carlo simulation using SRIM 2013 program. (a) shows the trajectories of ions and recoiling SiC atoms, (b) shows the distribution of silicon vacancy and carbon vacancy in depth direction.

The  $V_{Si}$  PL signal distributions in Fig. 5-6 indicate that the depth range where the defects can be detected is much larger than the 300 nm which would be somewhat expected from SRIM results in Fig. 7. Both the depth resolution of confocal spectroscopy and helium ion implantation induced swelling effect might result in the difference of defects' depth results by PL depth profiling and SRIM simulations.

The depth resolution of around 2  $\mu\text{m}$  for confocal Raman microscope [37] will mainly contribute to the detected widening of the defect distribution in depth direction.

### 3.2.4 Defect formation model

The three-dimensional analysis of the PL and Raman signals is helpful to reveal the actual distribution of silicon vacancies produced by helium ion implantation. From the presented results, we suggest the following model for the defect formation. Fig. 8(a) indicates that at doses lower than  $5.0 \times 10^{15}$  ions/cm<sup>2</sup>, damage exists in the form of point defects and concentrates in the central area. The swelling of the implanted region is no more than 7 nm. When the dose exceeds  $1.0 \times 10^{16}$  ions/cm<sup>2</sup>, as shown in Fig. 8(b), lenticular shaped helium bubbles form in the implanted area and the implanted area has been amorphized, as indicated by the gray region in Fig. 8(b). Larger helium bubbles are formed in the implanted center part and some helium bubbles connect with each other to form helium bubble clusters. At the junction of the ion-implanted area and the non-implanted area, the damage is not as large as the center part, and there are still point defects that can be detected by spectroscopy. Due to the formation of helium bubbles which contain a large amount of vacancies, the swelling effect is much more obvious than that at lower doses.

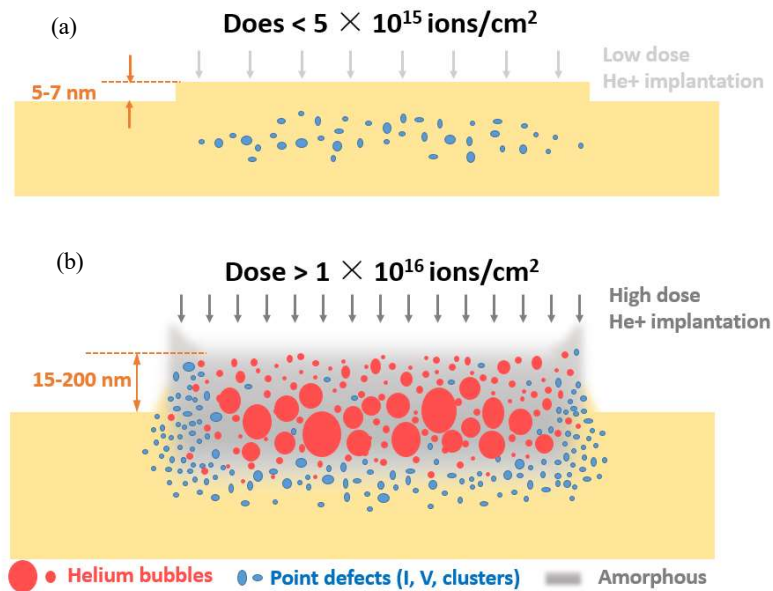


Fig. 8. Schematic diagram of defect distribution of helium ion implanted SiC with low dose (a) and high dose (b). (I stands for interstitial defects and V stand for vacancy defects.)

### 3.3 Crystalline defects

#### 3.3.1 Signals of C-C bond and Si-Si bond

Ion implantation induces damage in the crystal lattice, including point defects, lattice disorder and even amorphization at high doses, helium bubbles in case of He ion implantation, etc. In order to effectively control the quality of color centers, a higher concentration of color centers and low lattice disorder are required. Therefore, 532 nm and 638 nm lasers were used to excite the defects in He ion implanted 4H-SiC to study the lattice quality. As shown in Fig. 9(a), in addition to the Raman modes of 4H-SiC (FTA, E<sub>2</sub>, LOPC, second order Raman mode) [38,39], a peak located at 1390.8 cm<sup>-1</sup> was found under the excitation of 532 nm laser. And a peak located at 1383.2 cm<sup>-1</sup> was found under the excitation of 638 nm laser. These two signals were assigned to the sp<sup>2</sup>/sp<sup>3</sup> C-C bond vibration after the destruction of Si-C bond in 4H-SiC lattice by He ion implantation. After high-dose ion implantation, a signal of sp<sup>2</sup>/sp<sup>3</sup> hybrid C-C bond will appear near 1400 cm<sup>-1</sup> [25] and this hybrid peak is also called D peak (disorder induced peak) in amorphous carbon materials. Wolfgang discovered several signals in Raman spectroscopy that did not belong to SiC crystals, and attributed 480 cm<sup>-1</sup> to Si-Si bond, 800 cm<sup>-1</sup> to Si-C bond, and 1450 cm<sup>-1</sup> signals to C-C bond [40]. Sorieul et al. found a 1420 cm<sup>-1</sup> C-C bond signal in 6H-SiC after Au ion irradiation [41]. Ali et al. discovered the C-C bond signal near the second-order Raman peak of silicon carbide in 4H-SiC and 6H-SiC after He ion implantation [25]. Besides, D peak was found to have an excitation energy dependence, that is, the D peak will shift blue as the excitation energy decreases (or as the excitation wavelength increases) [26]. This coincides with the frequency shift of 7.6 cm<sup>-1</sup> of C-C bond we found here as the laser energy decreases from 2.33 eV (532 nm) to 1.94 eV (638 nm). The excitation energy dependence of C-C bond originates from the double resonance Raman scattering which is related to the special electronic energy band structure of graphite and other sp<sup>2</sup>-bonded carbon materials[42].

Fig. 9(b) and (c) shows the Raman spectra in regions with different implantation doses (R1-R9). The 4H-SiC signals of the E<sub>2</sub> and the LOPC mode drop gradually with increasing ion dose and nearly disappear when the ion dose exceeds 1.0×10<sup>17</sup> ions/cm<sup>2</sup> (R6). However, the signals of the E<sub>2</sub> mode and the LOPC mode recover again when the ion dose reaches 1.0×10<sup>18</sup> ions/cm<sup>2</sup> (R9), because the upmost implanted layer of the 4H-SiC substrate was mostly removed by the helium bubbles accumulation and helium ion sputtering, as shown in Fig. 1(e) and Fig. 2(g).

In the implanted region with a dose of 1.0×10<sup>17</sup> ions/cm<sup>2</sup> (R6), no second order Raman peaks were observed due to the high dose implantation induced lattice damages, whereas C-C bond defect peak located at 1390.8 cm<sup>-1</sup> appears. As the implantation dose increases, the intensity of C-C becomes stronger, which shows an accumulating lattice damage. Besides, as shown in Fig. 9(d), the signal around 480-520 cm<sup>-1</sup> at the excitation of 532 nm increases with the helium ion implantation dose, which is considered as the Si-Si bond [25]. With increasing implantation dose, the Si-Si bond Raman scattering signal shifts to lower wavelengths, which is consistent with the results from the literature [25].

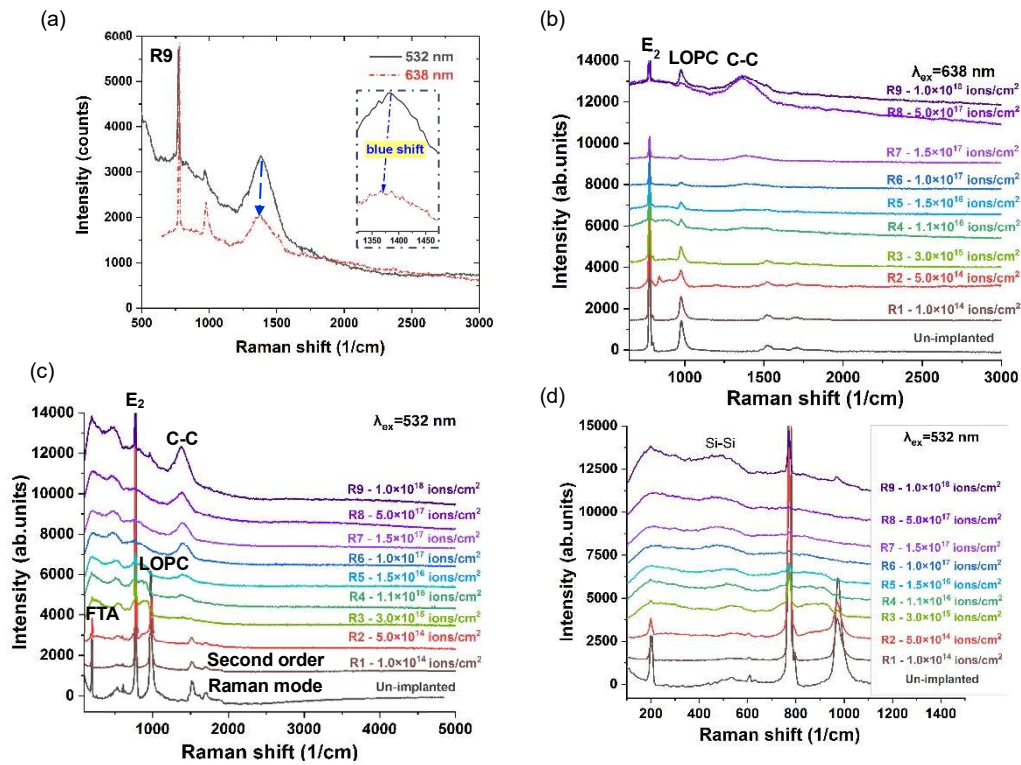


Fig. 9. Raman spectra of helium ion implanted 4H-SiC substrate excited by 532 nm and 638 nm laser. (a) Blue shift of C-C bond vibration when excited by different lasers in the helium ion implanted region of R9. (b) Raman spectra in regions with different implantation doses (R1-R9) excited by 638 nm laser. (c) Raman spectra in regions with different implantation doses (R1-R9) excited by 532 nm laser. (d) The Si-Si bond excited by 532 nm laser at different implanted doses.

### 3.3.2 2D mapping of E<sub>2</sub> mode and C-C bond with different doses

2D mapping of the Raman E<sub>2</sub> mode and C-C vibration mode was performed in the XY plane in SWIFT working mode to study the defect distribution and evaluate the uniformity of ion implantation and repeatability of single point spectrum measurement in Fig.9. Overall, the processing area is relatively uniform, which reflects the advantage of the ion implantation processing method, but there are some small intensity differences in the local area, which may be related to the uniformity of the silicon carbide substrate itself. Fig. 10 and Fig. 11 show the intensity distribution of the E<sub>2</sub> mode and the C-C vibration mode excited by 532 nm laser and 638 nm, respectively. As shown in Fig. 9(b-c), no obvious defect signal can be observed for R1 and R2. For the E<sub>2</sub> mode, which is related to the lattice integrity, the implanted region shows a weaker intensity than non-implanted area due to the ion implantation induced damage. On the contrary, for the C-C bond peak which is related to the lattice damage, the intensity in the implanted region is stronger than the intensity of the non-implanted region.

The C-C bond signal in the R8 region is significantly enhanced compared to R7 region and 638 nm excitation as shown in the 2D mapping image, which corresponds to the results in Fig. 9(b). For excitation of 532 nm, the significant enhancement of C-C bond can still be observed in the 2D mapping images of R7 and R8. But from the single point spectra in Fig. 9(c), there is not much difference of C-C bond intensity between R7 and R8. Therefore, in the case where the substrate is likely to be uneven, multi-point measurements or 2D mappings are recommended to evaluate the signal difference in different areas with higher reliability.

What is more, from R3-R6, there is no obvious increase in the 2D mapping results of the C-C bond signal as the dose increases (as shown in Fig. 10), but for the E<sub>2</sub> mode, the signal decreases with increasing dose which can be observed relatively clearly. The main reason is that the 2D mapping does not remove the baseline, but only presents the peak intensity distribution result of the local maximum intensity. And as the dose increases, the baseline increases (Fig. 9(b-c)). Moreover, the C-C bond signal in regions R3-R7 is relatively weak and the signal-to-noise ratio is smaller compared to the results of the E<sub>2</sub> mode. Therefore, the combined influence of baseline and signal-to-noise ratio results in no gradual increase in 2D imaging results of the C-C bond in R3-R7 regions.

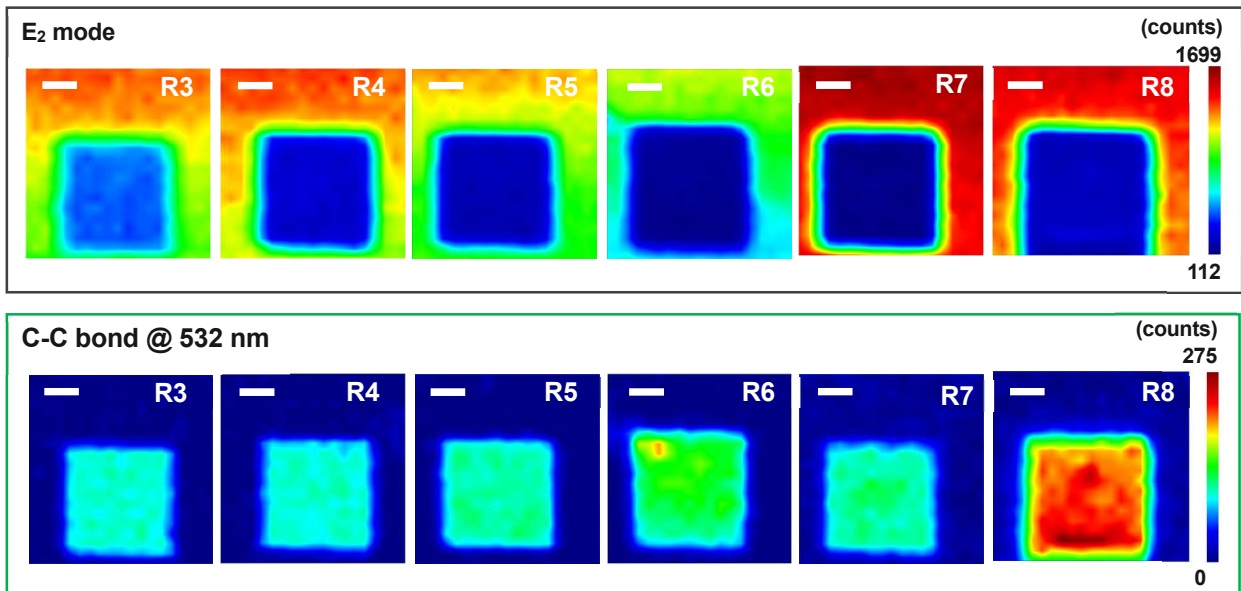


Fig. 10. Intensity distribution of  $E_2$  mode and C-C vibration mode excited by 532 nm laser when focusing on sample surface (scale bar is 2  $\mu\text{m}$ ).

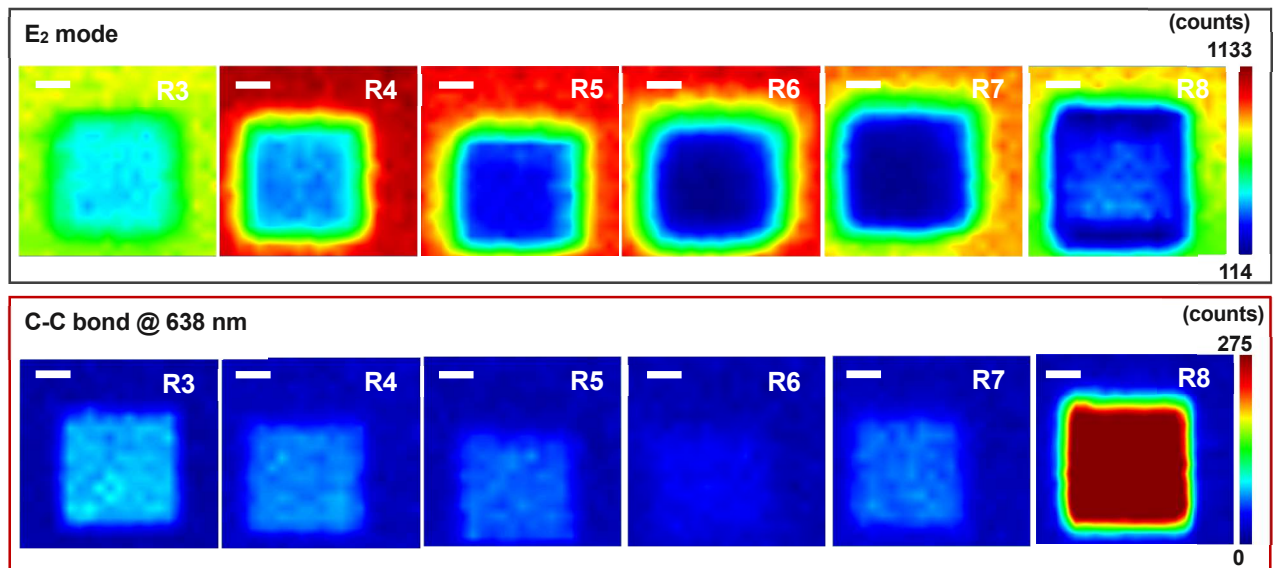


Fig. 11. Intensity distribution of  $E_2$  mode and C-C vibration mode excited by 638 nm laser (scale bar is 2  $\mu\text{m}$ ).

Then spectra for the R9 ( $1.0 \times 10^{18}$  ions/cm<sup>2</sup>) region were acquired and compared separately, as shown in the Fig. 12. For the  $E_2$  mode, the processed area gives smaller intensity than the unprocessed area, except for the three local parts where material removal has not occurred. In the central area, the rupture of the helium bubble causes the removal of the material. The absorption of light caused by helium bubbles is weakened, so more light can interact with the underlying material, and the  $E_2$  mode is stronger. As the upmost layer of the 4H-SiC substrate was mostly removed under such high ion implantation dose (see Fig. 1 e), the C-C bond intensities for both 532 nm and 638 nm excitation in the central area are both lower than those of the remaining area. Moreover, the C-C vibration signal shows nearly the same intensity distribution with three local intensity peaks.

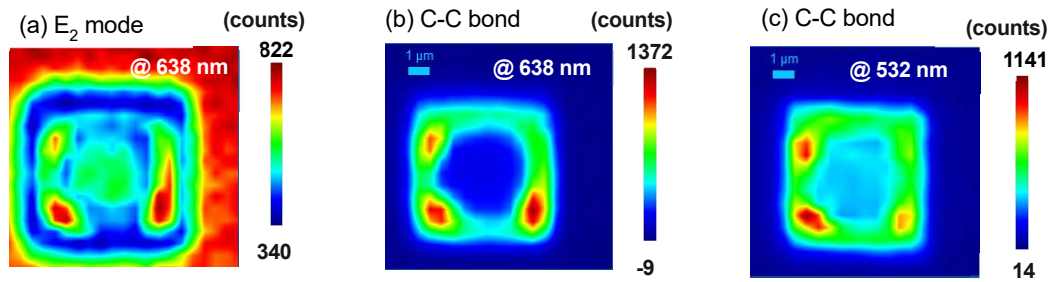


Fig. 12. Spectra results for sample R9 ( $1.0 \times 10^{18}$  ions/cm<sup>2</sup>). (a) Intensity distribution of E<sub>2</sub> mode; (b) C-C vibration signal excited by 638 nm laser; (c) C-C vibration signal excited by 532 nm laser.

#### 4. Conclusions

In this paper, defects of helium ion implanted n-type 4H-SiC were characterized by photo-luminescence (PL) and Raman spectroscopy at room temperature. PL peaks of V<sub>Si</sub> in the range of 850-950 nm were found for the excitation of both, 638 nm laser and 785 nm laser. According to the surface morphology by SEM and AFM and PL spectral characterization results, a defect formation model was established. When the implantation dose is below  $3.0 \times 10^{15}$  ions/cm<sup>2</sup>, V<sub>Si</sub> shows a higher intensity in the central part of the implanted area. And the swelling height is less than 7 nm by AFM. When the doses exceed  $1.0 \times 10^{16}$  ions/cm<sup>2</sup>, V<sub>Si</sub> shows an intensity pattern of weak center and strong edge of the ion-implanted area. Helium bubbles (Helium-vacancy complexes) form at high implantation doses and weaken the intensity of the V<sub>Si</sub> in the central part of the implanted area and induce severe swelling effect of around 15-200 nm. Besides, lattice defects like C-C bond and Si-Si bond were found in high dose ion-implanted area under the excitation of 532 nm and 638 nm. A blue shift of the C-C bond was observed when the laser wavelength increases from 532 nm to 638 nm. The difference between the depth profiling measurement results and SRIM simulation results was also explained by considering the confocal depth profile resolution and helium ion implant induced swelling effect.

#### ACKNOWLEDGEMENT

The study is supported by National Natural Science Foundation of China (No. 51575389, 51761135106), National Key Research and Development Program of China (2016YFB1102203), State key laboratory of precision measuring technology and instruments (Pilt1705), and the '111' project by the State Administration of Foreign Experts Affairs and the Ministry of Education of China (Grant No. B07014). The authors would like thanks to Mr. Qiang Li, Prof. Pengfei Wang, Prof. Jinshi Xu from University of Science and Technology of China for valuable discussions on this paper.

#### REFERENCES

1. Doherty MW, Manson NB, Delaney P, Jelezko F, Wrachtrup J, Hollenberg LCL (2013) The nitrogen-vacancy colour centre in diamond. *Physics Reports* 528 (1):1-45.
2. Awschalom DD, Hanson R, Wrachtrup J, Zhou BB (2018) Quantum technologies with optically interfaced solid-state spins. *Nat Photonics* 12 (9):516-527.
3. Luo H, Xu Z, Shi C, Hu M, Sun F, Shang L, Fang F (2019) Nanofabrication of Nitrogen-Vacancy Color Center. *Current Nanoscience* 15 (5):433-436.
4. Yang X, Yang X, Sun R, Kawai K, Arima K, Yamamura K (2019) Obtaining Atomically Smooth 4H-SiC (0001) Surface by Controlling Balance Between Anodizing and Polishing in Electrochemical Mechanical Polishing. *Nanomanufacturing and Metrology* 2 (3):140-147.
5. Zhai W, Gao B, Chang J, Wang H (2019) Optimization of Ultrasonic-Assisted Polishing SiC Through CFD Simulation. *Nanomanufacturing and Metrology* 2 (1):36-44.
6. Tarasenko SA, Poshakinskiy AV, Simin D, Soltamov VA, Mokhov EN, Baranov PG, Dyakonov V, Astakhov GV (2018) Spin and Optical Properties of Silicon Vacancies in Silicon Carbide-A Review. *physica status solidi (b)* 255 (1):1700258.
7. Soykal O, Reinecke TL (2017) Quantum metrology with a single spin-3/2 defect in silicon carbide. *Phys Rev B* (95):081405.
8. Widmann M, Lee SY, Rendler T, Son NT, Fedder H, Paik S, Yang LP, Zhao N, Yang S, Booker I, Denisenko A, Jamali M, Momenzadeh SA, Gerhardt I, Ohshima T, Gali A, Janzen E, Wrachtrup J (2015) Coherent control of single spins in silicon carbide at room temperature. *Nat Mater* 14 (2):164-168.

9. Lohrmann A, Johnson BC, McCallum JC, Castelletto S (2017) A review on single photon sources in silicon carbide. *Rep Prog Phys* 80 (3):034502.
10. Chen F, Zhao ER, Hu T, Shi Y, Sirbully DJ, Jokerst JV (2019) Silicon carbide nanoparticles as a photoacoustic and photoluminescent dual-imaging contrast agent for long-term cell tracking. *Nanoscale Advances* 1 (9):3514-3520.
11. Kraus H, Simin D, Kasper C, Suda Y, Kawabata S, Kada W, Honda T, Hijikata Y, Ohshima T, Dyakonov V, Astakhov GV (2017) Three-Dimensional Proton Beam Writing of Optically Active Coherent Vacancy Spins in Silicon Carbide. *Nano Lett* 17 (5):2865-2870.
12. Zargaleh SA, Hameau S, Eble B, Margailan F, von Bardeleben HJ, Cantin JL, Gao W (2018) Nitrogen vacancy center in cubic silicon carbide: A promising qubit in the 1.5 $\mu$ m spectral range for photonic quantum networks. *Phys Rev B* 98 (16):165203.
13. Castelletto S, Almutairi AFM, Kumagai K, Katkus T, Hayasaki Y, Johnson BC, Juodkazis S (2018) Photoluminescence in hexagonal silicon carbide by direct femtosecond laser writing. *Opt Lett* 43 (24):6077-6080.
14. Peng B, Jia RX, Wang YT, Dong LP, Hu JC, Zhang YM (2016) Concentration of point defects in 4H-SiC characterized by a magnetic measurement. *Aip Adv* 6 (9):095201.
15. Castelletto S, Johnson BC, Ivady V, Stavrias N, Umeda T, Gali A, Ohshima T (2014) A silicon carbide room-temperature single-photon source. *Nat Mater* 13 (2):151-156.
16. Koehl WF, Buckley BB, Heremans FJ, Calusine G, Awschalom DD (2011) Room temperature coherent control of defect spin qubits in silicon carbide. *Nature* 479 (7371):84-87.
17. Widmann M, Lee SY, Rendler T, Son NT, Fedder H, Paik S, Yang LP, Zhao N, Yang S, Booker I, Denisenko A, Jamali M, Momenzadeh SA, Gerhardt I, Ohshima T, Gali A, Janzen E, Wrachtrup J (2015) Coherent control of single spins in silicon carbide at room temperature. *Nature Materials* 14 (2):164-168.
18. Wang JF, Zhang XM, Zhou Y, Li K, Wang ZY, Peddibhoda P, Liu FC, Bauerdick S, Rudzinski A, Liu Z, Gao WB (2017) Scalable Fabrication of Single Silicon Vacancy Defect Arrays in Silicon Carbide Using Focused Ion Beam. *Acs Photonics* 4 (5):1054-1059.
19. Al Atem AS, Ferrier L, Canut B, Chauvin N, Guillot G, Bluet J-M (2016) Luminescent point defect formation in 3C-SiC by ion implantation. *Physica Status Solidi C* 13 (10-12):1-4.
20. Cottom J, Gruber G, Hadley P, Koch M, Pobegen G, Aichinger T, Shluger A (2016) Recombination centers in 4H-SiC investigated by electrically detected magnetic resonance and ab initio modeling. *Journal of Applied Physics* 119 (18):181507.
21. Li Q, Wang JF, Yan FF, Cheng ZD, Liu ZH, Zhou K, Guo LP, Zhou X, Zhang WP, Wang XX, Huang W, Xu JS, Li CF, Guo GC (2019) Nanoscale depth control of implanted shallow silicon vacancies in silicon carbide. *Nanoscale* 11 (43):20554-20561.
22. Wang J-F, Li Q, Yan F-F, Liu H, Guo G-P, Zhang W-P, Zhou X, Guo L-P, Lin Z-H, Cui J-M, Xu X-Y, Xu J-S, Li C-F, Guo G-C (2019) On-Demand Generation of Single Silicon Vacancy Defects in Silicon Carbide. *Acs Photonics* 6 (7):1736-1743.
23. Hijazi H, Li M, Barbacci D, Schultz A, Thorpe R, Gustafsson T, Feldman LC (2019) Channeling in the helium ion microscope. *Nuclear Instruments and Methods in Physics Research Section B: Beam Interactions with Materials and Atoms* 456:92-96.
24. Chu Y, de Leon NP, Shields BJ, Hausmann B, Evans R, Togan E, Burek MJ, Markham M, Stacey A, Zibrov AS, Yacoby A, Twitchen DJ, Loncar M, Park H, Maletinsky P, Lukin MD (2014) Coherent optical transitions in implanted nitrogen vacancy centers. *Nano letters* 14:1982-1986.
25. Ali AA, Kumar J, Ramakrishnan V, Asokan K (2018) Raman spectroscopic study of He ion implanted 4H and 6H-SiC. *Mater Lett* 213:208-210.
26. Vidano RP, Fischbach DB, Willis LJ, Loehr TM (1981) Observation of Raman band shifting with excitation wavelength for carbons and graphites. *Solid State Commun* 39 (2):341-344.
27. Stumpf F, Abu Quba AA, Singer P, Rumler M, Cherkashin N, Schamm-Chardon S, Cours R, Rommel M (2018) Detailed characterisation of focused ion beam induced lateral damage on silicon carbide samples by electrical scanning probe microscopy and transmission electron microscopy. *Journal of Applied Physics* 123 (12).
28. Tromas C, Audurier V, Leclerc S, Beaufort MF, Decl my A, Barbot JF (2008) Evolution of mechanical properties of SiC under helium implantation. *J Nucl Mater* 373 (1-3):142-149.
29. Leclerc S, Decl my A, Beaufort MF, Tromas C, Barbot JF (2005) Swelling of SiC under helium implantation. *Journal of Applied Physics* 98 (11):113506
30. Zhang CH, Donnelly SE, Vishnyakov VM, Evans JH (2003) Dose dependence of formation of nanoscale cavities in helium-implanted 4H-SiC. *Journal of Applied Physics* 94 (9):6017-6022.
31. Leclerc S, Beaufort MF, Decl my A, Barbot JF (2008) Evolution of defects upon annealing in He-implanted 4H-SiC. *Appl Phys Lett* 93 (12).
32. He Z, Liu T, Xu Z, Song Y, Rommel M, Fang F (2018) Investigation of Ga ion implantation-induced damage in single-crystal 6H-SiC. *Journal of Micromanufacturing* 1 (2):1-9.
33. Nakashima S, Harima H (1997) Raman Investigation of SiC polytypes. *physica status solidi (a)* 162:26.
34. Hain TC, Fuchs F, Soltamov VA, Baranov PG, Astakhov GV, Hertel T, Dyakonov V (2014) Excitation and recombination dynamics of vacancy-related spin centers in silicon carbide. *Journal of Applied Physics* 115 (13).
35. Ziegler JF, Ziegler MD, Biersack JP (2010) SRIM - The stopping and range of ions in matter (2010). *Nuclear Instruments and Methods in Physics Research Section B: Beam Interactions with Materials and Atoms* 268 (11-12):1818-1823.
36. Li R, Zhu R, Chen S, He C, Li M, Zhang J, Gao P, Liao Z, Xu J (2019) Study of damage generation induced by focused helium ion beam in silicon. *J Vac Sci Technol B* 37 (3):031804.
37. Tabaksblat R, Meier RJ, KIP BJ (1992) Confocal Raman Microspectroscopy: Theory and Application to Thin Polymer Samples. *Applied spectroscopy* 46:60-68.
38. Harima H, Nakashima Si, Uemura T (1995) Raman scattering from anisotropic LO-phonon-plasmon-coupled mode in n-type 4H- and 6H-SiC. *Journal of Applied Physics* 78 (3):1996-2005.

39. Feng M, Wang Y, Hao J, Lan G (2003) Raman Study of SiC Polytype Structure. Chinese Journal of light scattering 15:158-161.
40. Bolse W (1998) Formation and development of disordered networks in Si-based ceramics under ion bombardment. Nuclear Instruments and Methods in Physics Research B 141:133-139.
41. Sorieul S, Costantini JM, Gosmain L, Thomé L, Grob JJ (2006) Raman spectroscopy study of heavy-ion-irradiated  $\alpha$ -SiC. Journal of Physics: Condensed Matter 18 (22):5235-5251.
42. Reich S, Thomsen C (2004) Raman spectroscopy of graphite. Philos T R Soc A 362 (1824):2271-2288.